Energy-resolved intramultiplet mixing in the electron-volt range for $Ne^{**}\{(2p)^5(3p)\}$+He

W. Boom, S.S. Op de Beek, R.A.M.L. van Galen, F.J.J. Huijsmans, H.C.W. Beijerinck, and B.J. Verhaar

Physics Department, Eindhoven University of Technology, P.O. Box 513, 5600MB Eindhoven, The Netherlands

(Received 16 April 1993; revised manuscript received 28 January 1994)

We present time-of-flight measurements on fine-structure-changing $Ne^{**}\{(2p)^5(3p)\}$+He collisions in the energy range $200 \leq E \leq 1200$ meV. Absolute values of polarized-atom cross sections are given for six collision energies in this range for various transitions from the $\{\alpha_5\}$ and $\{\alpha_7\}$ initial fine-structure states with electronic angular momentum J_k=1, with $\{\alpha_l\} = \{(2p)^5(3p)_l\}$ and index l corresponding to the usual Paschen numbering within the multiplet with $l = 1$ through 10 with decreasing electronic energy. A wide range of energy dependencies of both cross-section magnitude and polarization effect is observed. Experimental results are compared with fully-quantum-mechanical coupled-channels calculations. Definite evidence is found for a serious shortcoming in both the input model potentials [D. Hennecart, Ph.D. thesis, Université de Caen, Caen, France, 1982 (unpublished); De Hennecart and F. Masnou-Seeuws, J. Phys. B **18**, 657 (1985)] and the semiclassical model as used by Manders *et al.* [Phys. Rev. A **39**, 4467 (1989)] for explaining the observed features in the thermal energy range.

PACS number(s): 34.20.−b, 34.50.Pi, 34.50.Fa, 35.80.+s

I. INTRODUCTION

In recent years the interest for inelastic collisions of short-lived electronically excited states is steadily growing [4–17]. In our crossed beam apparatus [18, 19] we determine absolute values of polarized-atom cross sections $Q_{l\leftarrow k}^{|M_k|}$ for the collision-induced intramultiplet mixing process

$$Ne^{**}\{(2p)^5(3p);\alpha_k, J_k, M_k\} + He \rightarrow Ne^{**}\{(2p)^5(3p);\alpha_l, J_l\} + He, \quad (1)$$

in which the different fine-structure levels $\{\alpha\}$ are short lived ($\tau \approx 20$ ns) and denoted by their Paschen numbers k and l, respectively. Furthermore, $|M_k|$ is the magnetic quantum number of the electronic angular momentum $\mathbf{J}_k$ of the initial state $\{\alpha_k\}$ with respect to the asymptotic relative velocity $\mathbf{g}$.

Recently, a hollow-cathode arc (HCA) source [20] for the neon species has been installed, supplementing the thermal metastable atom source [21] (TMS) and opening up the eV range of collisional energies. Initially, the aim was to look for possible differences between $^{20}Ne^{**}-{}^{(20)}Ne$ and $^{22}Ne^{**}-{}^{(20)}Ne$ cross sections due to symmetry effects [22], with smaller internuclear distances probed at superthermal energies. The notation $^{(20)}Ne$ is used for the natural mixture $^{20}Ne : {}^{22}Ne = 9 : 1$ of Ne isotopes with a majority of ^{20}Ne. A first measurement run for the Ne^{**}-He system, however, revealed large discrepancies between experimental and quantum-mechanical cross-section magnitudes [23]. Furthermore, the most prominent superthermal cross sections are unexplained by the current semiclassical model of Manders *et al.* [3]. These conclusions are all drawn from the comparison between TMS and HCA data. Measurements on the energy dependence of the cross-section magnitude and the polarization effect might provide more direct and definite evidence for a short coming in the semiclassical model.

With the TMS source, measurements on the energy dependence were performed earlier by varying the position of the scattering center [19]. As explained elsewhere [23], this method cannot be applied with the HCA source. However, due to its broad velocity distribution the HCA source is ideally suited for time-of-flight (TOF) measurements. This paper describes the operation and calibration of a TOF experiment with the newly installed HCA source and presents the experimental TOF results. The experimental setup is presented in Sec. II. In Sec. III the choice of TOF method and its parameters are discussed. Checks on the pseudorandom correlation method and the flight time calibration are described in Secs. IV and V, respectively. Aspects of the measuring routine and data analysis specific to TOF measurements are discussed in Sec. VI. The TOF results and comparison with quantum calculations are presented in Sec. VII. Definite evidence for a failing semiclassical model is given in Sec. VIII. Finally, the observed polarization asymmetry for the reverse $\{\alpha_5\} \leftrightarrow \{\alpha_7\}$ transition pair is discussed in Sec. IX. A semiclassical model is being developed and includes an additional "radial matching" mechanism at large internuclear distances, involving a change in the rotational quantum number of the relative nuclear motion. This implies a large sensitivity of the superthermal cross-section magnitudes to the details in the long-range part of the model potentials of Hennecart and Masnou-Seeuws [1, 2]. A small deficiency in these potentials can easily explain the observed discrepancies with the quantum results.

II. EXPERIMENTAL

A schematic view of the experimental setup is given in Figs. 1 and 2. Additional information on the ex-

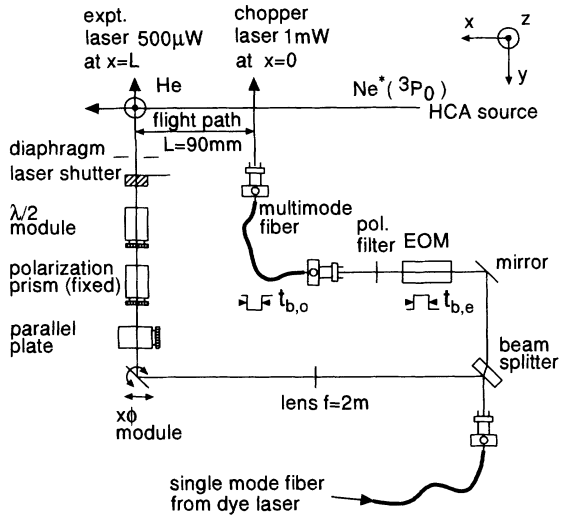

FIG. 1. Schematic view of the time-of-flight setup and method for the crossed beam experiment "minibeam I." The electronical and optical burst times are indicated by $t_{b,e}$ and $t_{b,o}$, respectively. A chopper burst of metastable atoms corresponds to a laser-off period. The origin of the xyz-coordinate frame is chosen at the nozzle exit of the secondary beam. EOM denotes an electro-optical modulator and HCA is a hollow-cathode arc source.

periment is given by Manders *et al.* [19] and specific aspects on the use of the HCA source by Boom *et al.* [23]. The scattering center is defined by the intersection at right angles of the primary, secondary and pump laser beams. The metastable neon atoms $Ne^*(^3P_0)$ of the primary beam are produced by the HCA source [20] and excited to one of the $Ne^{**}\{(2p)^5(3p)\}$ fine structure levels $\{\alpha_k\}$ by the linearly polarized pump laser. The short-lived atoms may collide with the helium atoms of the secondary beam, originating from a skimmerless supersonic expansion [24]. The optical detection system detects either "direct" fluorescence from the originally excited level or "indirect" fluorescence from a level $\{\alpha_l\}$ populated by collision-induced intramultiplet mixing. Narrow-band interference filters are used for wavelength selection. Both the $\{\alpha_5\}$ or $\{\alpha_7\}$ state have an electronic angular momentum $J_k = 1$ and are used as an initial state. Pure-state polarized-atom cross sections $Q_{l\leftarrow k}^{|M_k|}$ can then directly be measured in a parallel or perpendicular arrangement of the laser polarization and the asymptotic relative velocity $\mathbf{g}$.

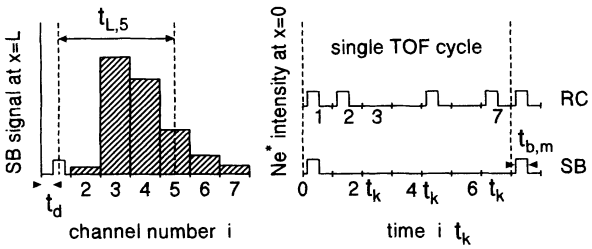

FIG. 2. Schematic view of the time-of-flight method. A chopper burst of metastable atoms corresponds to a laser-off period (Fig. 1). The Ne^* intensity at the position $x = 0$ of the chopper laser is given for both the SB and the pseudo-random correlation (RC) method. The response in the scattering center at $x = L$ is also shown for the SB method, integrated over the time channels i of the multiscaler. Both the metastable atom burst time $t_{b,m}$ and the delay time t_d are indicated, together with the mean flight time $t_{L,5}$ of the atoms detected in channel $i = 5$.

The optimum operating pressure for the secondary beam is given by the condition of an $1/e$ attenuation of the primary beam of metastable $Ne^*(^3P_0)$ atoms before it reaches the laser beam at the scattering center, as discussed by Manders *et al.* [19]. The attenuation of the beam of short-lived $Ne^{**}\{\alpha_k\}$ atoms is only 3% for an assumed (large) cross section $Q = 100$ Å^2, as follows from a typical value of the product $n_2\, l_\tau$ of the secondary beam density $n_2 = 3 \times 10^{20}$ m^{-3} and the path length $l_\tau = v_1\, \tau = 100$ μm at $v_1 = 5000$ m/s. The influence of depolarizing collisions *before* the inelastic transition and additional fine-structure changing collisions *after* the inelastic transition considered is thus negligible. This has also been checked experimentally by varying the secondary beam operating pressure [19]. The $Ne^{**}\{\alpha_k\}$ are thus investigated at near ideal single collision conditions, in spite of the large attenuation of the beam of metastable atoms upstream of the scattering center.

Inevitable to the compact minibeam setup is the use of a laser chopper to perform TOF measurements. The short flight path $L = 90$ mm in combination with the high velocity $v_1 \simeq 5000$ m/s of the primary beam atoms requires correspondingly short chopper pulses and a correspondingly accurate synchronization between chopper and counting device. Furthermore, a laser chopper is favored for its compactness and for an easy implementation of either the single burst (SB) or the pseudorandom correlation (RC) method.

The dye laser beam arriving at the minibeam experiment is split into a chopper beam and a pump beam for the production of the short-lived Ne^{**} atoms in the scattering center. The chopper beam can be switched on and off by an electro-optical modulator (EOM) followed by a polarizer. A short multimode fiber is used to transport the chopper beam to the desired position along the primary beam axis. The chopper beam depletes the primary beam of metastable $Ne^*(^3P_0)$ atoms by optical pumping. A pulse of $Ne^*(^3P_0)$ atoms transmitted by the chopper thus corresponds to a laser-off period. For the chopper laser we use a power of 1 mW. With an effective diameter of 1.5 mm this corresponds to a saturation parameter $s_0 = 13$ and 16 for the wavelengths $\lambda = 626.6$ nm and 653.3 nm of the $Ne^*(^3P_0) \rightarrow Ne^{**}\{\alpha_5\}$ and $Ne^*(^3P_0) \rightarrow Ne^{**}\{\alpha_7\}$ optical transitions, respectively. The interaction time with the chopper laser beam for atoms with a velocity $v_1 = 10\,000$ m/s is equal to 150 ns, corresponding to 8 τ and 7.3 τ, respectively. The branching ratio for the decay of the $\{\alpha_5\}$ and $\{\alpha_7\}$ states to the resonant states of the $Ne^*\{(2p)^5(3p)\}$ multiplet is equal to 0.50 and 0.58, repectively. Combining these data with the saturation parameter we can conclude that the typ-

TABLE I. Parameters for the velocity distribution of primary beam flux obtained by a least-squares analysis of the SB TOF spectrum in Fig. 3 using the model function of Eq.(2).

u	S	γ_3	γ_4	γ_5	γ_6
4825	1.95	-3.58×10^{-2}	5.10×10^{-2}	-1.03×10^{-2}	0.231×10^{-2}

ical value of the experimentally observed attenuation of 93–96 % is in good agreement with the laser parameters.

The central part of the time-of-flight experiment is the multiscaler with a minimum channel time $t_k = 500$ ns. The multiscaler both accumulates the fluorescence signal counts in its time channels (bit 1–15) and supplies the corresponding series of chopper pulses (bit 16). At initialization, a preprogrammed pseudo-random or single burst series can be downloaded. After initialization, up to a maximum of 65 000 TOF cycles can be accumulated by the multiscaler itself, after which the M68000 computer [25], that controls the experiment, is notified to sample the data and eventually to restart the cycle.

The transistor-transistor logic (TTL) chopper output pulses pass an extra digital delay line before going to a 250 V switching amplifier to drive the EOM. The time constant of 60 ns is mainly determined by the pulse transformers used to galvanicly decouple the high voltage stage of the amplifier from the TTL input part.

A high resolution SB TOF spectrum of the direct fluorescence is shown in Fig. 3, taken with $t_k = 1$ μs. A suitable model function for the velocity distribution of the primary beam flux is given by [26]

$$P(v_1)dv_1 = Cv_1e^{-\zeta^2}\left[1+\sum_{n=3}^{6}\gamma_n H_n(\zeta)\right]dv_1,$$
$$\zeta = S\left(\frac{v_1-u}{u}\right), \qquad (2)$$

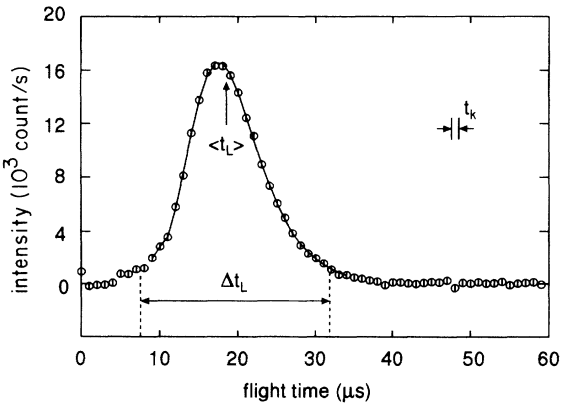

FIG. 3. High resolution SB TOF spectrum of the direct fluorescence with channel time $t_k = 1$ μs . The solid line represents the curve fit with the model function $P(v_1)$ of Eq.(2) and the parameters of Table I. The average flight time $\langle t_L\rangle$, total spread in flight times Δt_L and channel time t_k are indicated.

in which v_1 is the primary beam velocity, S the speed ratio between the flow velocity u and the local thermal velocity α in the moving frame and C a normalizing constant. The Hermite polynomials H_n correct for the skewness and kurtosis of the distribution. The results of a least-squares analysis are given in Table I.

III. TOF METHOD AND PARAMETERS

First, we must decide which TOF method is to be preferred. With the SB TOF method, single chopper bursts are used to measure the time-delay spectrum directly. With the RC TOF method a pseudo-random maximum length sequence with $N_c = 2^m - 1$ (m =0,1,2,...) elements is used to define the chopper function of N_c time channels. The time-delay spectrum is obtained after cross correlation of the experimental RC TOF spectrum with this pseudo-random sequence. The RC TOF method has the advantage of a much higher duty cycle than the SB TOF method. However, (the square of) the statistical error is the same for all channels and is proportional to the total number of accumulated signal counts in all channels. For the SB TOF method only the number of signal counts in each separate channel determines the statistical error for that channel. A fair choice between both TOF methods can be made by comparing the relative errors η for both time-delay spectra [derived from work of Beijerinck [27], using the approximation $(N_c+1)/N_c \approx 1$]:

$$\left(\frac{\eta_i^{\mathrm{RC}}}{\eta_i^{\mathrm{SB}}}\right)^2 = \frac{4}{N_c}\frac{(1+\frac{1}{2}\kappa)}{(1+\delta_i\kappa)},$$
$$\kappa = \frac{s}{b}, \qquad (3)$$

with δ_i the fraction of the time-delay distribution in the time-delay channel with index i. The quantities s and b are the signal and background count rates with a nonchopped primary beam, which follow from the usual type of polarization effect measurement [19, 23]. In most cases the signal to background ratio $\kappa < 1$ and the ratio $(\eta_i^{\mathrm{RC}}/\eta_i^{\mathrm{SB}})^2$ is mainly determined by the factor $4/N_c$. Already for $N_c = 7$ the RC TOF method is to be preferred.

Second, a choice for t_k is to be made. The velocity distribution and flight path L determine the average flight time $\langle t_L\rangle = 18$ μs and the total spread in flight times $\Delta t_L = 25$ μs (see Fig. 3). The channel time t_k now determines the TOF resolution $(t_k/\langle t_L\rangle)$ and the number of signal channels $(\Delta t_L/t_k)$ in the time-delay spectrum. In a crude approximation each of these signal channels contains a fraction $\delta_i = (t_k/\Delta t_L)$ of the time delay distribution. A choice for δ_i, thus implicitly for t_k, is made by considering the relative error η_i^{RC}, given by

$$\left(\eta_i^{\mathrm{RC}}\right)^2 = \frac{4}{T\,\delta_i^2\,\kappa^2\,b}\left(1+\tfrac{1}{2}\kappa\right), \tag{4}$$

with T the total measuring time. Note the quadratic relationship between T and the quantities η_i^{RC}, δ_i, and κ ($\kappa < 1$). This forces us to make a careful choice for these quantities in order to maintain an acceptable value for the total measuring time. Choosing five signal channels ($\delta_i \approx 0.2$ and $t_k = 5$ μs) and taking η_i^{RC}=2.5%, we find $T = 1$ h for a typical case with $\kappa = 0.5$ and $b = 200$ cps.

Since N_c itself is absent in Eq.(4), its value is arbitrary for the RC TOF method, as long as the full time-delay distribution is contained in N_c channels. We choose $N_c = 2^4 - 1 = 15$, the first available value larger then the minimal value N_c=12 that is required to contain the full time-delay distribution with $t_k = 5$ μs. Because the choice for δ_i—and thus for the channel time t_k—is fully determined by the trade-off between the required relative error η_i^{RC} and the total acceptable measuring time T, it is not useful to increase the number of channels N_c to a larger value. For $N_c = 15$ already sufficient time channels are available for an accurate calculation of the background.

IV. PSEUDO-RANDOM CORRELATION

The pseudo-random correlation method is prone to systematic errors, as has been shown by other authors [28–32]. In view of the preference for the RC TOF method to measure the "indirect" fluorescence, it is of paramount importance that we carefully check our method. Zero flight path measurements with $L = 0$ are essential as a calibration tool to reveal systematic errors. The chopper beam then crosses the primary beam in the scattering center with the pump beam blocked. Either the laser light scattered from the elevated nozzle or the "direct" fluorescence can be used.

Chopper pulse shape identity is crucial for reliable random correlation measurements. Each pulse should have an identical effect, irrelevant whether it is preceeded by an "on" or "off" cycle. Deviations from the chopper function defined with the pseudo-random sequence are enlarged by the cross correlation with the exact, downloaded pseudo-random sequence. The final result is an additional contribution in the time-delay spectrum. By assuming a constant variation Δ_{ch} added to the either 0 or 1 valued chopper function, we can estimate the magnitude of this extra term. For the time-delay channel i we find

$$D_i/S_i = 2\Delta_{\mathrm{ch}}/N_c\delta_i \tag{5}$$

for the ratio between the additional contribution D_i and the signal contribution S_i to the total content C_i of the time-delay channel after cross correlation. Note that both terms are cross correlation sums of TOF spectra and that the background contribution B_i does not play any role.

In the multiscaler the channel time t_k is derived from an external clock $t_{\mathrm{clk}} = t_k/10$. Within a channel, the electronical burst time $t_{b,e}$ can be defined in units of $t_k/5$ up to 80% of the total channel time t_k. This allows a recovery time between adjacent chopper pulses, so that chopper pulse shape identity can be achieved. Rigorous experimental tests are required to verify this.

Pulse shape effects are clearly demonstrated in a RC measurement with $L = 0$, in which the response is a direct image of the chopper function. After cross correlation, we expect a SB chopper burst, i.e., a signal dip in the first channel and a constant laser-on (=chopper closed) level in the other channels. An observed variation of 25 ns on both edges of electronical pulses with a width of $t_{b,e}$=1600 ns now directly gives a variation of 2.5% in the "constant" level (N_c=15, scattered light). This closely agrees to the estimate of 2.9% according to Eq.(5) with $\delta_i = 1/(N_c - 1)$.

Choosing burst periods of 60% for channel times of $t_k = 5$ μs results in electronically indistinguishable RC high voltage pulses. Variation in either the laser on or off channels separately of the $L = 0$ RC TOF spectrum is only 0.1%. After cross correlation a variation of 0.5% results for the "constant" level. The shape identity of the high voltage pulses is mainly limited by the frequency response of the pulse transformers that are used in the switching amplifier.

As a final check on the implementation of the RC TOF method, an RC and SB TOF spectrum are measured of the direct fluorescence in a short time period of about 15 min. After cross correlation, the two experimental spectra represent the same time-delay distribution. More specifically, time channels of both spectra with the same channel number exactly correspond with each other. The ratio of their countrates should therefore be constant and equal to the ratio of the duty cycles $2/(N_c + 1)$, after a careful subtraction of the background in both cases. We find an acceptable ratio of 0.1269±0.0005 for channels 3–8 with $N_c = 15$. Previous to this final check, many experiments have been performed involving different pseudo-random sequences, different values of N_c, and different channel times t_k. All these experiments support the conclusions of the final check presented here.

V. FLIGHT TIME CALIBRATION

A correct measurement of the delay time t_d and the effective burst time $t_{b,m}$ of the metastable atom burst is important for an accurate value of the flight time, and thus the primary beam velocity v_1. Furthermore, accurate values for t_d and $t_{b,m}$ are required for a correct treatment of convolution effects due to the finite burst and channel times. Convolution effects are important due to the small number of channels used. Finally, we want to compensate t_d to capture the zero flight path response in a single channel. This allows a simple interpretation of the time-delay spectrum after cross correlation and allows a rigorous test on (unwanted) "ghost" effects. The hardware has two features for delay time compensation. First, a coarse adjustment is possible by backshifting the pseudo-random sequence by a number of channels. Second, a fine adjustment is provided by a digital delay line. This is a fast 10-bit TTL shift register, using the same

clock as the multiscaler. The extra time delay t_s due to this device can be varied manually between 0 and t_k in units of $t_k/10 = t_{\rm clk}$.

A. Delay time

The value of t_d is determined in an $L = 0$ SB TOF measurement, detecting scattered laser light from the nozzle and using an interference filter. The timing diagram is shown in Fig. 4. The chopper output pulse is chosen to start simultaneously with the gating of the first time channel $i = 1$. The delay time t_d is defined as the difference between the gating of the first time channel and the actual response in the detection, i.e., the moment when the count rate at the multiscaler drops due to the single burst interruption of the laser beam. Note that t_d also includes the extra time delay t_s of the delay line, but that the difference $(t_d - t_s)$ is determined by the apparatus only and should be independent of either t_s, t_k, or the relative electronical burst time $t_{b,e}/t_k$. During the determination of t_d only, the shift register is used to spread the response of the chopper burst over the first two channels (see Fig. 4). The ratio $r_{12} = S_1/S_2$ between the countrate decreases for both channels is the ratio between the two parts of the chopper burst. The sum of both decreases is divided by the countrate difference between the laser permanently on and off, to give the effective optical burst time $t_{b,o}/t_k$. The delay time t_d is now given by

$$t_d = t_k - \frac{r_{12}}{(1 + r_{12})} t_{b,o} \, . \tag{6}$$

It has been verified that $(t_d - t_s)$ does not depend on t_s, t_k, or $t_{b,e}/t_k$. The obtained value $(t_d - t_s)_{\rm expt}$=490 ns is in reasonable agreement with the estimated value $(t_d - t_s)_{\rm calc}$=440 ns, based on the delay times of the separate components listed in Table II. Finally, we find $t_{b,o}/t_k$=0.59, compared to $t_{b,e}/t_k$=0.6 .

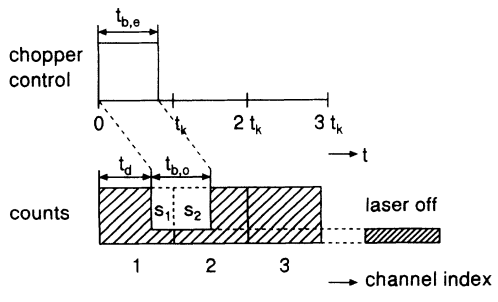

FIG. 4. Timing diagram for the $L = 0$ SB TOF measurement of the delay time t_d. An interference filter is used to detect the scattered chopper laser light from the elevated nozzle. The single burst interruption of the chopper laser results in a countrate decrease for the first two channels, indicated by S_1 and S_2, respectively. The ratio $r_{12} = S_1/S_2$ directly gives the ratio between the two chopper burst parts. The sum $S_1 + S_2$ is used to determine the optical burst time $t_{b,o}$.

B. Pulse width

When using "direct" fluorescence instead of scattered laser light, the above method can also be applied to measure the effective burst time $t_{b,m}$ of the metastable atom burst. However, we first checked for both cases if the zero flight path response can correctly be captured in the first channel. The result of both $L = 0$ SB TOF measurements is given in Table III. Since a chopper burst corresponds to a laser-off period, a dip in the photon signal results. For the measurement with scattered laser light, the effect of the single burst is indeed purely restricted to the first channel. This means that the delay time t_d is correctly compensated. For the direct fluorescence case, however, an "overshoot" in the second channel is evident.

This "overshoot" can easily be understood. In the stationary situation optical pumping only occurs in the upstream part of the laser intersection with the primary beam. The downstream part is fully depleted of metastable neon atoms. However, when the laser is switched off during a chopper burst, the latter region is also filled with metastable neon atoms. In a minimum burst time of 300 ns, a metastable atom moving at 4800 m/s, travels a distance of 1.4 mm, comparable to the chopper laser waist of about 1.5 mm. Switching the laser on again, results in a temporary increase of the direct fluorescence countrate, because optical pumping now occurs over the full laserwidth. In a similar way, the finite laserwidth also causes the burst time $t_{b,m}$ of the metastable atom pulse to be shorter than the optical burst time $t_{b,o}$, by optical pumping of the "tail" of the metastable neon atom pulse. We conclude that an explicit determination of $t_{b,m}$ is necessary and that a method similar to the t_d,$t_{b,o}$ determination cannot be applied. In that case, particularly, t_d is strongly dependent on t_s, t_k, and $t_{b,e}/t_k$.

For the determination of $t_{b,m}$ we therefore use the reference measurements on the direct fluorescence, alternating the actual TOF measurements. The chopper laser is then situated at its intended position 90 mm upstream of the scattering center. A reference measurement consists among others of a countrate measurement with the chopper laser permanently switched on or off using an ordinary scaler and a countrate measurement with the TOF multiscaler using either an on or off series of chopper bursts. The pulse width $t_{b,m}/t_k$ is now equal to the ratio of the countrate differences for the multiscaler and the scaler measurements. A shortening $t_{b,o} - t_{b,m} = 270 \pm 60$ ns of the burst time is observed independent of t_k = 1,2,5,10 μs. As shown above, this shortening is fully explained by the pumping of the metastable atom burst over the width of the chopper laser beam, at the moment the chopper laser is switched on again. If a cylindrical lens is temporarily placed in the chopper beam, the shortened laser width indeed results in a smaller value for $t_{b,o} - t_{b,m} = 130 \pm 40$ ns, also independent of t_k. Finally, we note that the average velocity for the TMS source is about five times as small as for the HCA source. In that case a shortening of at least 1 μs is expected and both the experiment and the analysis should very carefully take account of this shortening.

TABLE II. Delay times of the separate components in the TOF setup.

Component	Delay time (ns)
Cable from multiscaler to amplifier	125
Switching amplifier	160
Photomultiplier (electron transit time)	45
Pulse amplifier and discriminator (PARC 1182)	50
Cable from amplifier to multiscaler	30
Multiscaler	30
Estimated total delay time	440

C. Ghost Phosphorescence

We have also performed an $L = 0$ SB TOF measurement with a cutoff filter as an analyzer for the scattered laser light from the nozzle (Table III). The "undershoot" in the second channel for this case is presumably due to a phosphorescence process in the experimental apparatus, unrevealed when using interference filters due to their small spectral acceptance. This is confirmed in a separate measurement, where the EOM is temporarily adjusted so that a chopper burst corresponds to a laser-on period. Furthermore, a maximum time delay t_s is applied with no signal pulses detected in the next channel for the corresponding measurement with an interference filter. A phosphorescence "echo" of about 8% in the next channel now shows up, nearly independent of t_k, indicating a linear dependence on the exposure time. For this reason the cut off filters have not been used for the TOF measurements.

VI. MEASURING ROUTINE AND DATA ANALYSIS

In a non-energy-resolved measurement [19] a set of four different measurements is performed in order to correct for background light from the metastable atom source and the laser and direct fluorescence "leakage" through the filters used for collision induced fluorescence. For this the laser is put on and off resonance and the secondary beam is switched on and off. Since the direct fluorescence "leakage" is negligible for the HCA source [23] and the background light contribution is obtained from the background channels, only one type of TOF measurements is necessary, namely, that with the laser on resonance and the secondary beam switched on.

In order to supress drift effects, the TOF measurements are divided into independent blocks of 1/2 h measuring time, in which spectra for both the direct and indirect fluorescence are measured in an alternating sequence. Typical signals and measuring times for the $\{\alpha_7; |M_7| = 0\} \rightarrow \{\alpha_5\}$ transition are presented in Table IV.

Since both direct and indirect fluorescence are measured at the same spot, using the same optical detection sytem, the direct and indirect fluorescence time channels with the same index exactly correspond with each other. The data analysis for each separate time-delay channel is therefore similar to that for a non-energy-resolved measurement [19, 23]. We therefore restrict ourselves to only those features of the data analysis specific for TOF measurements.

An important issue is the determination of the relative velocity g by which the ratio of indirect and direct fluorescence is to be divided to obtain the absolute cross section. Due to the small number of signal channels in the time-delay spectrum ($\Delta t_L/t_k \approx 5$), the time-delay distribution function may vary significantly within a channel and an elaborate procedure is required to obtain an average g_i and a standard deviation σ_i^g for the relative velocity in channel i=1,2,...,N_c . The (unnormalized) primary beam flux distribution $F_i(v_1)$ corresponding to the accumulated signal in channel i is given by (flux $\sim$ count rate for both direct and collision-induced fluorescence)

TABLE III. Zero flight path ($L = 0$) single burst TOF spectra for various conditions. Only the normalized channel content of the first five channels are given. A laser wavelength $\lambda_l = 627$ nm is used. Either the scattered laser light by the elevated nozzle or the "direct" fluorescence is detected, either by a 2 nm bandpass interference filter at 671 nm or by a red glass 665 nm cutoff filter. Timing parameters are $t_k = 1$ μs, $t_d = 1.31$ μs, and $t_{b,o} = 0.55$ μs for the first two and $t_k = 5$ μs, $t_d = 0.93$ μs, and $t_{b,o} = 2.88$ μs for the latter two TOF measurements.

Light source	Filter type	Chan 1	Chan 2	Chan 3	Chan 4	Chan 5
Scattered laser light	interference	0.38	1.00	1.00	1.00	1.00
Direct fluorescence	interference	0.65[a]	1.05	1.00	1.0	1.00
Scattered laser light	interference	0.43	1.00	1.00	1.00	1.00
Scattered laser light	cutoff	0.47	0.98	1.00	1.00	1.00

[a]The background increase by the HCA source for all channels causes the relative difference between the first and the following channels to decrease.

TABLE IV. Typical signals and measuring times for the $\{\alpha_7; |M_7| = 0\} \rightarrow \{\alpha_5\}$ transition[a] using the HCA source and the RC TOF method.

Quantity	Direct fluorescence	Indirect fluorescence
Number of recorded TOF spectra[a]	5×10^6	21×10^6
Measuring time (minutes)[c]	7	27
Total number of counts in top channel[d]	8.10×10^6	2.9×10^5
Total number of counts in background channel	4.52×10^5	1.48×10^5

[a] s = 180 counts/s, b=100 counts/s, κ=1.8, $t_{b,e}/t_k$=0.6, δ_{top}=0.35.
[b] N_c=15, t_k=5, μs, 2 measuring blocks.
[c] Total elapsed time 50 minutes; each of the 12 reference measurements takes $\approx$ 2 min.
[d] Actual cross section $Q^{|0|}_{5\leftarrow7}$ E=350±50 meV)=3.85±0.05.

$$F_i(v_1)\,dv_1 = P(v_1)\,A(it_k - t_d - t_L; t_k, t_{b,m})\,dv_1,$$
$$t_L = L/v_1. \tag{7}$$

Here $P(v_1)$ is the normalized flux distribution for a continuous primary beam, t_L the flight time corresponding to v_1 and A a transmission function taking into account both the finite channel time t_k and burst time $t_{b,m}$. This transmission function has a trapezium shape in the time domain (see Fig. 5) and is given analytically by

$$A(it_k - t_d - t_L; t_k, t_{b,m}) = \frac{\min[(it_k - t_d - t_L), t_{b,m}]}{t_{b,m}} - \frac{\max[(it_k - t_d - t_L) - t_k, 0]}{t_{b,m}}, \tag{8}$$

in which A is positive or zero otherwise. After proper normalization of $F_i(v_1)$ for each separate channel i, the function $F_i(v_1)$ is used to determine

$$g_i = \langle g \rangle_i, \tag{9}$$
$$\sigma_i^g = \langle g^2 \rangle_i - \langle g \rangle_i^2, \tag{10}$$

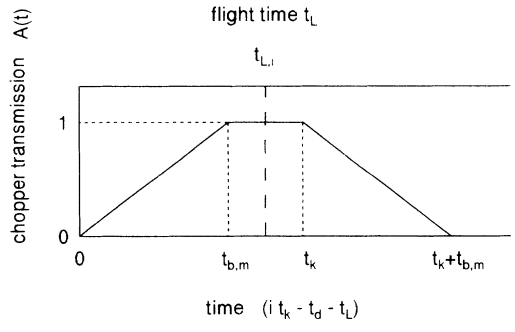

FIG. 5. Transmission function $A(it_k - t_d - t_L; t_k, t_{b,m})$ as a function of $(it_k - t_d - t_L)$, taking into account the finite channel time t_k and burst time $t_{b,m}$. For this case $t_{b,m} < t_k$. The upper horizontal scale gives the flight time t_L, with the central flight time $t_{L,i}$ of channel i corresponding to the symmetry axis of the transmission function A.

for channel i by averaging $g = |\mathbf{v}_1 - \mathbf{v}_2(\mathbf{x}_{sc})|$, in which $\mathbf{v}_1 = v_1\mathbf{e}_x$ and $\mathbf{v}_2$ is the secondary beam velocity at the position $\mathbf{x}_{sc}$ of the scattering center. In order to have a consistent relation between the relative velocity and the collision energy, the latter is defined as $E_i \pm \sigma_i^E = \frac{1}{2}\mu g_i^2 \pm \mu g_i \sigma_i^g$.

In Fig. 6 the values of g_i are compared with the relative velocity calculated from the flight times

$$t_{L,i} = (i - 1/2)t_k - (t_d + t_{b,m}/2), \tag{11}$$

obtained by using the center position of both time channel and chopper burst. Evident is the shift in g towards the value corresponding to the top of the distribution. This shift is most prominent for the high velocity channels where the primary beam velocity v_1 changes most rapidly as a function of the flight time. The bar graph in Fig. 6 represents the time-delay spectrum. The

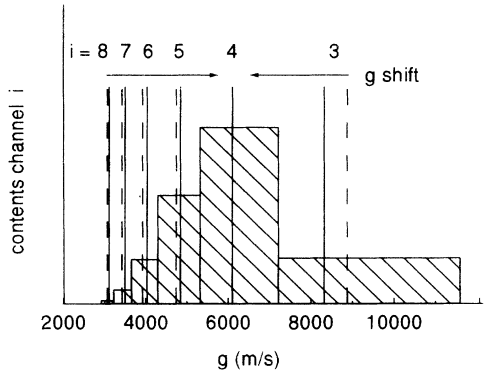

FIG. 6. Comparison between averaged values g_i (solid vertical lines) of the relative velocity for channel i and values obtained by taking central flight times $\tau_{L,i}$ according to Eq.(11) (dotted vertical lines). A shift of the g values towards the value corresponding to the top of the distribution in channel 4 is observed. Experimental values used for the calculation are $\mathbf{x}_{sc}$=(0,0,2) mm, v_2 = 1700 m/s, t_k = 5 μs, t_d = 0.8 μs, and $t_{b,m}/t_k$ = 0.54. The bar graph represents the time delay spectrum, with the height of the bars corresponding to the integral of the unnormalized functions $F_i(v_1)$ [Eq.(7)] for each channel i. The bar borders correspond to the flight time $t_{L,i} \pm t_k/2$ at the border of the time channel.

bar heights are obtained by integrating the unnormalized functions $F_i(v_1)$ over v_1 for each separate channel. The bar borders represent the relative velocities corresponding with the borders of the time channels and the middle of the chopper burst, i.e., flight times $t_L = t_{L,i} \pm t_k/2$.

A second issue concerns the polarization effect. The change in magnitude of $\mathbf{v}_1$ over the various channels causes the orientation of $\mathbf{g} = \mathbf{v}_1 - \mathbf{v}_2$ to vary. Relevant for the polarization effect is now the angle β between $\mathbf{g}$ and the laser polarization. Time-of-flight spectra are only recorded for the two angles β, 90° apart, at which the non-energy-resolved cross section is extremal. A deviation α_i from both of these angles results in a smaller polarization effect to be measured for channel i. However, because for each channel the 90° difference in β between both TOF measurements still holds, the pure state polarized atom cross section $Q^{|M_k|}(E_i)$ can be retrieved from the measured cross sections $Q_i^{'|M_k|'}$ in the following way (J_k=1):

$$Q^{|M_k|}(E_i) = \frac{(Q_i^{'|M_k|'} + Q_i^{'|1-M_k|'})}{2} + \frac{(Q_i^{'|M_k|'} - Q_i^{'|1-M_k|'})}{2\cos(2\alpha_i)}. \quad (12)$$

For reasons of consistency, the orientation of $\mathbf{g}$, used to determine the angle α_i, is derived from v_2, g_i, and $\mathbf{x}_{sc}$. In Fig. 7 measured and pure state polarized atom cross sections are compared for the $\{\alpha_7\} \rightarrow \{\alpha_5\}$ transition. For this transition the largest polarization effect is observed, so that the largest corrections are made. Especially for the low velocity channels, where v_1 becomes comparable to v_2, the correction takes on importance.

A final issue is the convolution factor ξ, by which the ratio of indirect and direct fluorescence is divided [19, 23]. This factor is obtained in a numerical simulation of the experiment and takes into account the finite size of the scattering center, the details of the optical pumping process, the spread in the velocity distributions, and the dependence of the cross section Q on g. This dependence strongly influences the value of ξ. A least-squares curve fit with a second order polynomial on the data obtained in the first order TOF analysis is used as an estimate for the actual dependence of Q on g. A channel-dependent convolution factor ξ_i is obtained by using a primary beam density distribution proportional to $F_i(v_1)/v_1$ instead of $P(v_1)/v_1$. All ξ_i are referred to the corresponding g_i and to the same $\mathbf{x}_{sc}$ = (0,0,2) mm and v_2, which are used in the first order data analysis. Note that the average position $\mathbf{x}_{sc,i}$ of the scattering center, weighed by the collision induced fluorescence distribution function, also varies with the channel index i. By choosing a fixed reference position $\mathbf{x}_{sc}$, the convolution factor ξ_i also contains the effect of this positional change and the different ξ_i values can directly be compared. We find a typical range $0.85 \leq \xi_i \leq 0.95$. For a specific transition the variation in ξ_i over the different channels is at most a few percent, contrary to $\mathbf{x}_{sc,i}$, which varies typically from −0.15 to −0.4 mm.

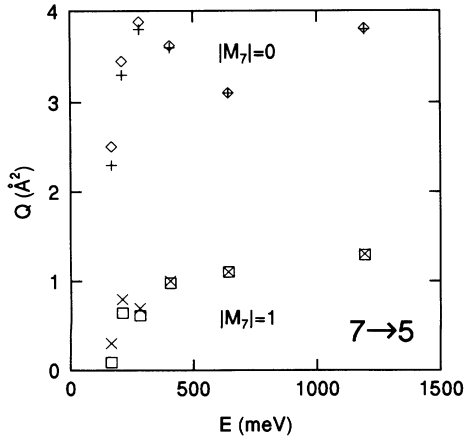

FIG. 7. Measured (+/×) and corrected (◇/□) polarized-atom cross sections for the $\{\alpha_7\} \rightarrow \{\alpha_5\}$ transition as a function of the collision energy.

VII. TOF RESULTS

The experimental TOF results for collision induced intramultiplet mixing in the Ne**−He system at superthermal energy are presented in Figs. 8–13. Both the $\{\alpha_5\}$ and $\{\alpha_7\}$ $J_k = 1$ levels are used as an initial state. Only the $\{\alpha_5\} \rightarrow \{\alpha_4, \alpha_6\}$ transitions are measured using the SB TOF method, the first only for the laser polarization corresponding to $|M_k| = 0$. The experimental results are also listed in Tables V (random correlation time-of-flight

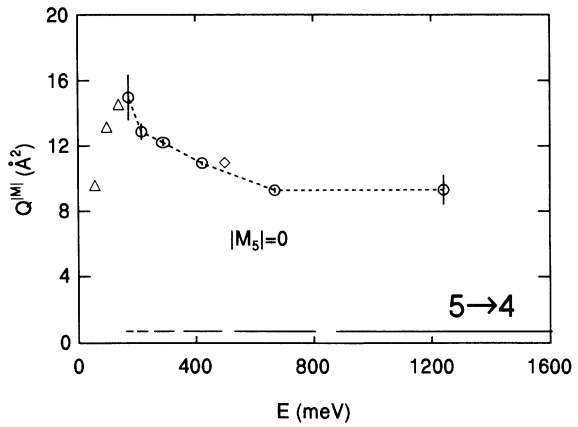

FIG. 8. The polarized atom cross section $Q^{|0|}_{4\leftarrow5}$ as a function of the collision energy E. Circles (○) indicate the measured SB TOF data, triangles (△) and diamonds (◇) thermal (Refs. [33 and 3]) and superthermal (Ref. [23]) data, respectively, from previously reported, non-energy-resolved measurements of the polarization effect. The strong decrease of the cross-section magnitude with increasing energy is unexplained by the current semiclassical model. Note the relatively large value of the cross-section magnitude. Vertically, statistical errors only are indicated. The error bars representing the energy spread in each time channel for the single burst time-of-flight (SB TOF) method are indicated directly above the horizontal axis. The drawn curves are included only as a guide to the eye.

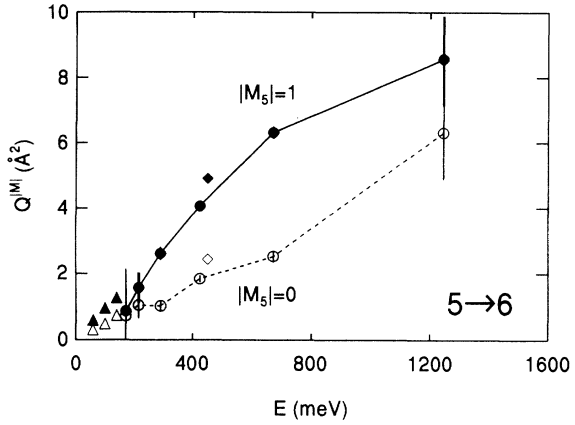

FIG. 9. The polarized atom cross sections $Q_{6\leftarrow 5}^{|M_5|}$ as a function of the collision energy E. Open and full symbols correspond to $|M_5|$=0 and $|M_5|$=1, respectively. Circles (○) indicate the measured SB TOF data, triangles (△) and diamonds (◇) thermal (Refs. [33,3]) and superthermal (Ref. [23]) data, respectively, from previously reported, non-energy-resolved measurements of the polarization effect. Vertically, statistical errors only are indicated. The drawn curves are included only as a guide to the eye.

method) and VI (single burst time of flight method). In this section we describe the main features of the experimental data set and make a first comparison with fully-quantum-mechanical coupled channels calculations.

The horizontal error bars of the TOF data points represent the (calculated) spread in collision energy σ_i^E of the data points is indicated by horizontal error bars directly above the horizontal axis, both for the single burst (SB) and the random correlation (RC) time-of-flight method. This spread in collision energy is only indicated in the first figure relating to either the SB (Fig. 8) or the RC method (Fig. 10). Due to the $t \rightarrow v$ transformation this spread increases for the lower channel numbers, i.e., high collision energies. The vertical error bars represent the statistical error only. Larger statistical errors are found in both wings of the time-delay distribution and for the smaller cross sections in general.

A rich spectrum of energy dependencies of the polarized-atom cross-sections is observed. Globally, the cross-section magnitude varies between 0.5 and 14 Å^2. The strongest increase in magnitude is observed for the $\{\alpha_7\} \rightarrow \{\alpha_6\}$ transition with $|M_k| = 0$, and amounts to a factor 11 (Fig. 13). The strongest decrease in magnitude amounts to a factor 2 and is observed for the

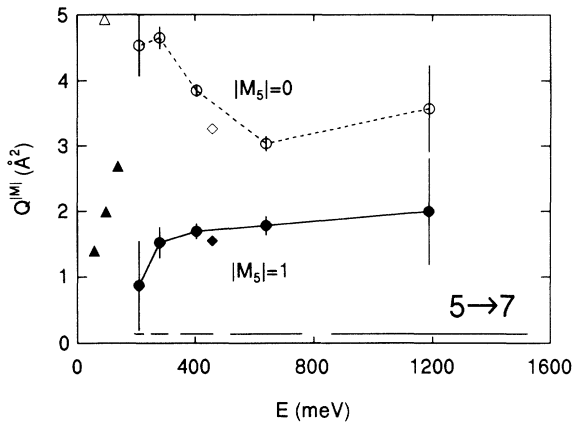

FIG. 10. The polarized atom cross sections $Q_{7\leftarrow 5}^{|M_5|}$ as a function of the collision energy E, measured with the RC TOF method. Open and full symbols correspond to $|M_5|$=0 and $|M_5|$=1, respectively. Circles (○) indicate the measured RC TOF data, triangles (△) and diamonds (◇) thermal (Refs. [33 and 3]) and superthermal (Ref. [23]) data, respectively, from previously reported, non-energy-resolved measurements of the polarization effect. The interconnection between thermal and superthermal data is far from smooth. No explanation for this is available yet. The error bars representing the energy spread in each time channel for the random correlation time-of-flight (RC TOF) method are indicated directly above the horizontal axis. Vertically, statistical errors only are indicated. The drawn curves are included only as a guide to the eye.

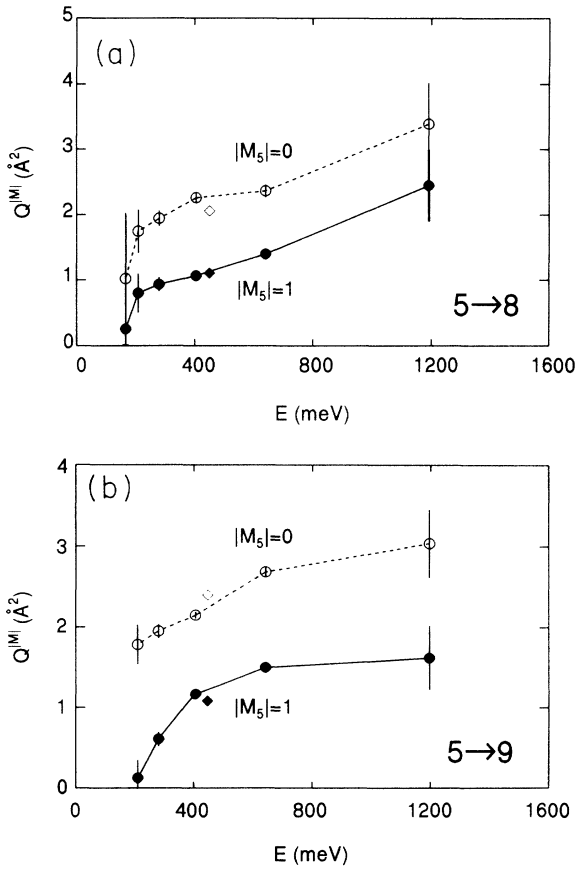

FIG. 11. The polarized atom cross sections $Q_{8,9\leftarrow 5}^{|M_5|}$ as a function of the collision energy E, measured with the RC TOF method. The conventions of Fig. 10 also apply here. Note the similarity between the experimental results for both transitions.

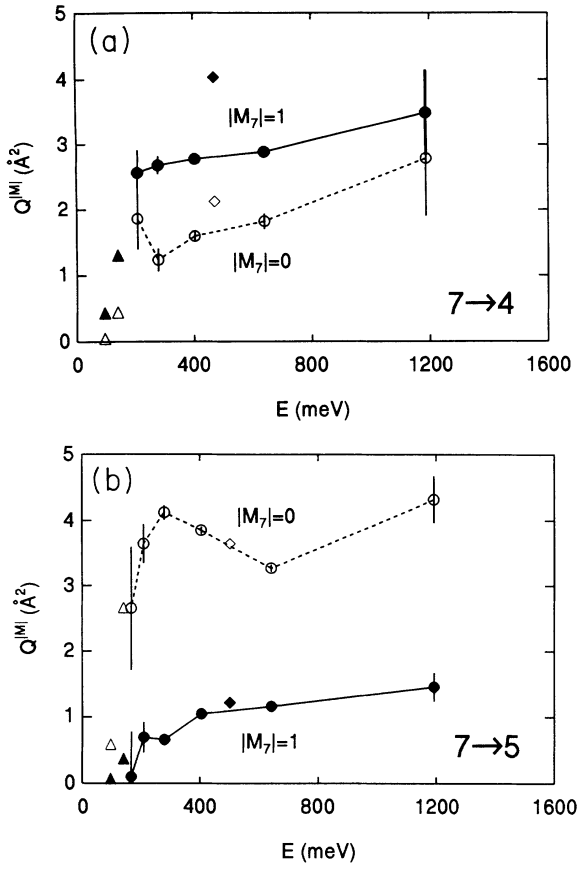

FIG. 12. The polarized atom cross sections $Q^{|M_7|}_{4,5\leftarrow 7}$ as a function of the collision energy E, measured with the RC TOF method. The conventions of Fig. 10 also apply here. The threshold behavior of the $\{\alpha_7\} \rightarrow \{\alpha_4, \alpha_5\}$ transitions is due to the endothermicity of the transition. Note the considerable polarization effect at high energy for the $\{\alpha_7\} \rightarrow \{\alpha_5\}$ transition, in contrast with the almost vanishing polarization effect for the reversed $\{\alpha_5\} \rightarrow \{\alpha_7\}$ transition.

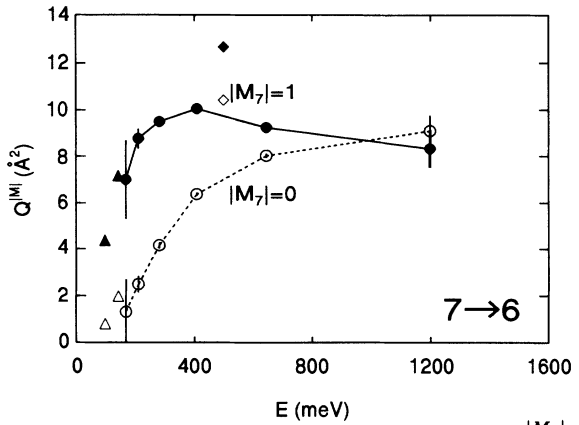

FIG. 13. The polarized atom cross sections $Q^{|M_7|}_{6\leftarrow 7}$ as a function of the collision energy E, measured with the RC TOF method. The conventions of Fig. 10 also apply here. Both the energy dependence of the cross-section magnitude and the polarization effect are fully unexplained by the current semiclassical model. Note the relatively large value of the cross section magnitude.

$\{\alpha_5\} \rightarrow \{\alpha_7\}$ transition with $|M_k| = 0$ (Fig. 10). For the $\{\alpha_7\} \rightarrow \{\alpha_5\}$ transition with $|M_k| = 0$ a clear local maximum is present (Fig. 12).

For comparison, the results [23] of the usual type of non-energy-resolved, polarization effect measurement are also given, yielding averages over the relative velocity distribution. The average collision energy for these measurements varies between 450 and 500 meV. Furthermore, no ξ correction is made for these measurements. A fair agreement is found with the TOF data. The $\{\alpha_7\} \rightarrow \{\alpha_6\}$ transition is an exception in this respect, see Fig. 13. Possibly, this might be attributed to the observed strong energy dependence of the polarized-atom cross sections.

Previously reported [33,3] thermal data are also given. These data are obtained by the usual type of polarization effect measurement, using the TMS source. Thermal collision energies range from 60 to 140 meV. In most cases, thermal and superthermal data points can smoothly be interconnected. In this respect we note that at thermal energy a correct value of the collision energy is of paramount importance when comparing experimental and quantum results. Due to the sharp increase in cross-section magnitude, a possible 10% experimental uncertainty in g, i.e., a 20% difference in collision energy, can result in a variation by a factor 2 in the quantum cross-section magnitude.

Only for the $\{\alpha_5\} \rightarrow \{\alpha_7\}$ transition no smooth interconnection between thermal and superthermal data points is possible. As a check, an explicit comparison between the SB and RC TOF method is made for this transition and presented in Figs. 14. The agreement between the results of both methods is reasonable, certainly in view of the measuring time for the SB method, which amounted to several hours. This leaves the nonsmooth interconnection unexplained sofar. The small differences in collision energy between the data points of both methods are due to the different choice $t_{b,e}/t_k = 0.8$ for the SB method as compared to $t_{b,e}/t_k = 0.59$ for the RC TOF method (Sec. V A). In spite of the longer measuring time

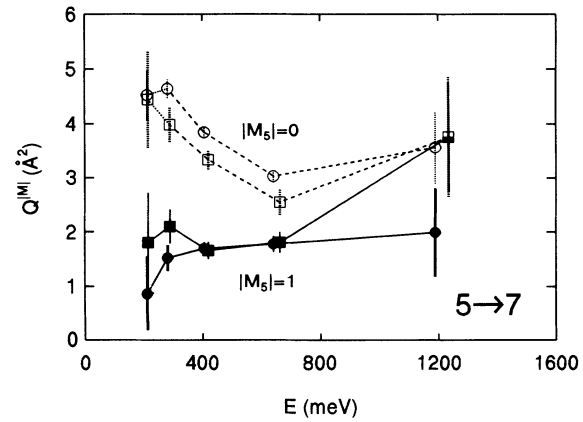

FIG. 14. Comparison between the polarized atom cross sections $Q^{|M_5|}_{7\leftarrow 5}$ measured either with the RC method (○) or the SB method (□). Agreement is reasonable, certainly in view of the long measuring time for the SB data.

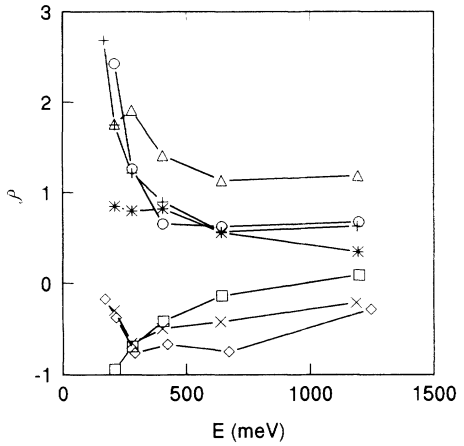

FIG. 15. Energy dependence of the polarization effect, expressed by the anisotropy parameter $\mathcal{P}$, for all transitions studied with the TOF method: ◇ 5→6 (SB), + 5→7, * 5→8, ○ 5→9, × 7→4, △ 7→5, □ 7→6. A broad range of polarization effects and energy dependencies is observed.

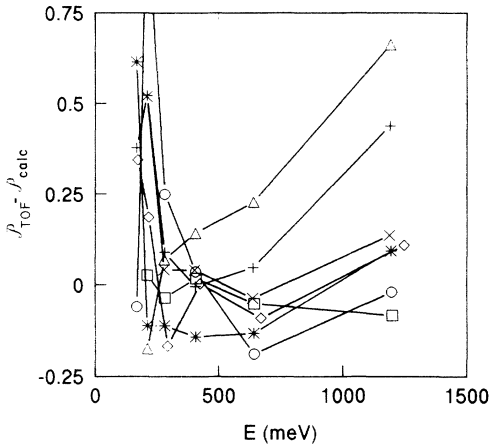

FIG. 16. Comparison between the experimental and the quantum-mechanical polarization effect as a function of the collision energy for all transitions studied with the TOF method: ◇ 5→6 (SB), + 5→7, * 5→8, ○ 5→9, × 7→4, △ 7→5, □ 7→6. Generally, agreement is excellent and mostly within $|\mathcal{P}^{\rm expt} - \mathcal{P}^{\rm calc}|=0.25$.

and the larger $t_{b,e}/t_k$ ratio, the statistical errors are still definitely larger for the SB method.

The polarization effect is expressed by the anisotropy parameter $\mathcal{P}$ [23], defined as

$$\mathcal{P} = [(Q^{|0|}_{l\leftarrow k} - Q^{|1|}_{l\leftarrow k})]/Q_{l\leftarrow k} ,$$
$$Q_{l\leftarrow k} = (Q^{|0|}_{l\leftarrow k} + 2Q^{|1|}_{l\leftarrow k})/3 , \quad (13)$$

with $Q_{l\leftarrow k}$ the unpolarized-atom cross section. An

TABLE V. Experimental results for the polarized-atom cross sections $Q^{|M|}_{l\leftarrow k}$ for $(k=5, l=7,8,9)$ and $(k=7, l=4,5,6)$, both for $|M|=0$ and 1, for the six energies of the hollow-cathode arc. The data have been obtained using the pseudo-random correlation (RC) time of flight method. The numbers between parentheses indicate the rms spread in the collision energy and the statistical error in the cross section, respectively. For comparison, results for previously reported, non-energy-resolved measurements in the superthermal (Ref. [23]) energy range are also given.

Initial		Final	RC method, collision energy E (meV)					
k	$\|M\|$	l	170 (12)	210 (17)	280 (30)	405 (57)	640 (120)	1190 (330)
5	0	7		4.53 (0.47)	4.65 (0.17)	3.85 (0.10)	3.03 (0.12)	3.57 (0.67)
5	0	7				3.26[a]		
5	1	7		0.87 (0.68)	1.52 (0.24)	1.69 (0.12)	1.78 (0.15)	1.99 (0.81)
5	1	7				1.55 [a]		
5	0	8	1.02 (1.01)	1.74 (0.33)	1.94 (0.12)	2.26 (0.06)	2.36 (0.10)	3.39 (0.63)
5	0	8				2.05 [a]		
5	1	8	0.25 (0.88)	0.80 (0.30)	0.93 (0.11)	1.06 (0.06)	1.40 (0.09)	2.45 (0.55)
5	1	8				1.10 [a]		
5	0	9		1.78 (0.25)	1.95 (0.09)	2.15 (0.04)	2.69 (0.06)	3.04 (0.42)
5	0	9				2.35 [a]		
5	1	9		0.13 (0.22)	0.61 (0.09)	1.17 (0.04)	1.50 (0.06)	1.62 (0.40)
5	1	9				1.08 [a]		
7	0	4		1.86 (0.46)	1.24 (0.17)	1.59 (0.09)	1.82 (0.12)	2.79 (0.89)
7	0	4				2.13 [a]		
7	1	4		2.56 (0.35)	2.68 (0.14)	2.78 (0.08)	2.89 (0.09)	3.49 (0.65)
7	1	4				4.03 [a]		
7	0	5	2.65 (0.94)	3.65 (0.30)	4.12 (0.11)	3.85 (0.05)	3.27 (0.05)	4.32 (0.35)
7	0	5				3.64 [a]		
7	1	5	0.10 (0.68)	0.69 (0.23)	0.66 (0.08)	1.05 (0.04)	1.16 (0.04)	1.46 (0.21)
7	1	5				1.21 [a]		
7	0	6	1.30 (1.39)	2.48 (0.35)	4.15 (0.12)	6.36 (0.07)	8.02 (0.09)	9.08 (0.67)
7	0	6				10.39 [a]		
7	1	6	7.00 (1.69)	8.75 (0.43)	9.48 (0.15)	10.04 (0.08)	9.23 (0.11)	8.31 (0.79)
7	1	6				12.65 [a]		

[a]Non-energy-resolved measurements at an energy E=(470±300) meV (Ref. [23]).

TABLE VI. Experimental results for the polarized-atom cross sections $Q_{l\leftarrow k}^{|M|}$ for ($k = 5, l = 4, 6, 7$), both for $|M| = 0$ and 1, for the six energies of the hollow-cathode arc. The data have been obtained using the SB time-of-flight method. The numbers between parentheses indicate the rms spread in the collision energy and the statistical error in the cross section, respectively. For comparison, results for previously reported, non-energy-resolved measurements in the superthermal (Ref. [23]) energy range are also given.

Initial		Final	SB method, collision energy E (meV)					
k	$\|M\|$	l	172 (12)	215 (19)	290 (34)	425 (65)	670 (140)	1240 (365)
5	0	4	14.97 (1.38)	12.87 (0.49)	12.20 (0.21)	10.93 (0.12)	9.27 (0.16)	9.31 (0.91)
5	0	4				11.00[a]		
5	1	4				12.19 [a]		
5	0	6	0.72 (1.07)	1.04 (0.39)	1.02 (0.18)	1.84 (0.10)	2.52 (0.17)	6.31 (1.43)
5	0	6				2.45 [a]		
5	1	6	0.86 (1.27)	1.57 (0.46)	2.61 (0.20)	4.06 (0.13)	6.31 (0.18)	8.57 (1.43)
5	1	6				4.90 [a]		
5	0	7		4.45 (0.88)	3.99 (0.32)	3.33 (0.18)	2.55 (0.23)	3.76 (1.01)
5	0	7				3.26 [a]		
5	1	7		1.80 (0.92)	2.10 (0.32)	1.65 (0.16)	1.81 (0.19)	3.76 (1.10)
5	1	7				1.55 [a]		

[a]Non-energy-resolved measurements at an energy E=(470±300) meV (Ref. [23]).

overview containing all measured TOF values of $\mathcal{P}$ is given in Fig. 15. A broad range of polarization effects and energy dependencies is observed. In general, $\mathcal{P}$ tends towards zero for increasing energy, though considerable polarization effects can still be found. The strongest energy dependencies of $\mathcal{P}$ are found for the $\{\alpha_7\} \rightarrow \{\alpha_6\}$ transition ($\mathcal{P} > 0$) and the $\{\alpha_5\} \rightarrow \{\alpha_7\}$ transition ($\mathcal{P} < 0$), respectively.

A comparison between experimental and quantum-mechanical polarization effects and cross-section magnitudes is presented in Figs. 16 and 17, respectively. In spite of the broad range of occuring $\mathcal{P}$ values, experimental and calculated polarization effects agree excellently, mostly within $|\mathcal{P}^{\text{expt}} - \mathcal{P}^{\text{calc}}|$=0.25. The cross-section magnitude, however, discloses discrepancies ranging from

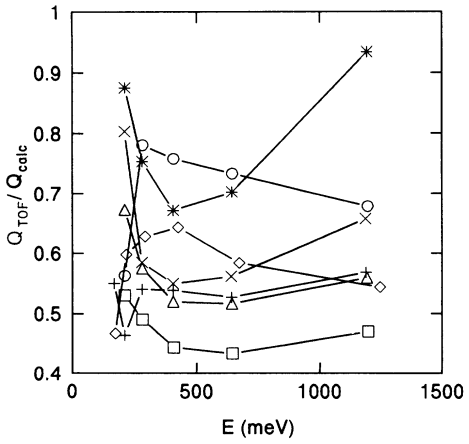

FIG. 17. Comparison between experimental and quantum-mechanical cross-section magnitude as a function of the collision energy for all transitions studied with the TOF method: ◇ 5→6 (SB), + 5→7, * 5→8, ○ 5→9, × 7→4, △ 7→5, □ 7→6. Large discrepancies are present.

$Q_{l\leftarrow k}^{\text{calc}}/Q_{l\leftarrow k}^{\text{expt}} = 0.45$–$0.8$.

Compared to the much stronger energy dependencies $Q_{l\leftarrow k}^{\text{expt}}$ and $\mathcal{P}$ that are observed, this means that the general shape of the energy dependence, including threshold effects and local maxima, is qualitatively reproduced. A similar conclusion was drawn for the non-energy-resolved polarization effect measurements earlier [23].

VIII. ENERGY DEPENDENCE AND FAILING SEMICLASSICAL MODEL

In the analysis of the non-energy-resolved polarization effect measurements the existence of an additional "radial matching" transition mechanism was suggested [23]. In the current semiclassical model transitions are only possible at localized avoided crossings between adiabiatic potentials. These are all situated in the "inner" part of the potential, i.e., at internuclear distances $R < 9a_0$. The "radial matching" mechanism now involves a change in the rotational quantum number of the relative motion of the two nuclei at large internuclear distances. Rotational energy is used to bridge the electronic energy difference. The existence of such a transition mechanism is supported by quantum calculations. In a number of cases these show significant cross-section contributions for impact parameters up to $12a_0$, far beyond the relevant crossing radius. This also implies that "radial matching" is a very efficient transition mechanism, i.e., results in the largest cross-section magnitudes found. Furthermore, such a mechanism implies a large sensitivity of the superthermal cross-section magnitudes on the details of the longe-range part of the potential. The discrepancy between experimental and quantum cross-section magnitudes may, therefore, be ascribed to a deficiency in the long-range part of the model potentials used. A semiclassical model incorperating the additional "radial matching" transition mechanism is being developed. In

this paper, we confine ourselves to demonstrating that the TOF technique, disclosing the energy dependence of the cross section, provides more definite evidence on the existence of this additional transition mechanism.

In the current semiclassical model, the single pass transition probability p_{kl} to switch between the adiabatic k and l states is given by the Landau Zener formula

$$p_{kl} = \exp(-v_{kl}/v_{\rm rad}), \tag{14}$$

in which $v_{\rm rad}$ is the local radial velocity and v_{kl} a reference velocity, characterizing the avoided crossing [34]. Furthermore, the semiclassical model uses a locking radius R_L to switch between a space fixed and a body fixed description of the electronic angular momentum **J**. For $R > R_L$ the **J** vector remains space fixed, resulting in a purely geometrical redistribution over the different Ω states along the trajectory. For $R < R_L$ the intermolecular forces "lock" **J** to the internuclear axis and Ω is a conserved quantum number.

$\{\alpha_7\} \rightarrow \{\alpha_6\}$ *transition.* The $\{\alpha_7\} \rightarrow \{\alpha_6\}$ transition is due to an avoided crossing in the $\Omega = 1$ manifold at $R_x = 7.4a_0$. With $R_x \approx R_L \approx 7a_0$, the crossing is bound to be met twice along a full trajectory. Due to the low reference velocity $v_{67} = 165$ m/s compared to the average relative velocity $g = 5000$ m/s, the probability p_{67} to switch between adiabatic states is close to unity. However, a net transition is achieved by switching only once from k to l state, either on the in or out going transit. Clearly, for a net transition to occur, the probability $(1 - p_{67})$ to follow the adiabatic potential is the limiting factor. Since this probability decreases further with increasing $v_{\rm rad}$, we expect a clear decrease in cross-section magnitude with rising superthermal collision energy. The opposite is observed in Fig. 13, with the $\{\alpha_7\} \rightarrow \{\alpha_6\}$ transition showing the strongest increase in cross-section magnitude of all measured transitions.

The energy dependence of the polarization effect cannot be understood either on the basis of the current semiclassical model. Due to the small reference velocity, we expect a clear preference for impact parameters close to the crossing radius ("grazing collision"), with the lowest attainable local radial velocity. When decomposing the original space-fixed orientation $|M_J|$ of **J** into local body-fixed Ω components at $R = R_L$ for these impact parameters, a pure $|M_J|$ state is decomposed into a scrambled mix of Ω states. With the transition due to an avoided crossing in the Ω=1 manifold specifically, we expect a small polarization effect $|\mathcal{P}|$ in this case. Even "polarization inversion" is possible, with the space-fixed $|M_J|$=0 state corresponding with a projection Ω=1 upon the local internuclear axis and otherwise for the $|M_J|$=1 state. Clearly, we then expect the polarization effect to be inversed. No significant inversion of the polarization effect is observed however. Furthermore, the polarization effect present is considerable and vanishes only at about 1 eV. Clearly, this cannot be accounted for by the current semiclassical model. Finally, we note that since the polarization effect is small where the cross section is large, the non-energy-resolved polarization effect measurement only reveals a small polarization effect. Here the TOF technique shows its value.

In Fig. 18 the quantum-mechanical partial cross section $dQ^{\Delta N}_{6\leftarrow 7}/db$ is given as a function of the impact parameter b for the possible (even) changes

$$\Delta N = N_l - N_k \tag{15}$$

of N at collision energies E=90, 150, and 1000 meV, respectively. Already at 90 meV the onset of a contribution at large impact parameters is observed, which is unmistakebly present at 150 meV and forms the dominant cross-section contribution at 1000 meV. A clear preference for $\Delta N = -2$ is displayed, even for the intermediate b range 4 a_0-8 a_0 at the thermal collision energy E=150 meV.

$\{\alpha_5\} \rightarrow \{\alpha_4\}$ *transition.* The $\{\alpha_5\} \rightarrow \{\alpha_4\}$ transition is due to an avoided crossing in the $\Omega = 1$ manifold with an even lower reference velocity v_{54}= 20 m/s. Practically, $p_{45} = 1$. In order to make a net transition, the geometric redistribution over the Ω states between the crossing radius $R_x = 8.6$ and the locking radius $R_L \approx 7a_0$ is required to prevent a second transit of the crossing. This redistribution is determined only by the orientation of **J**

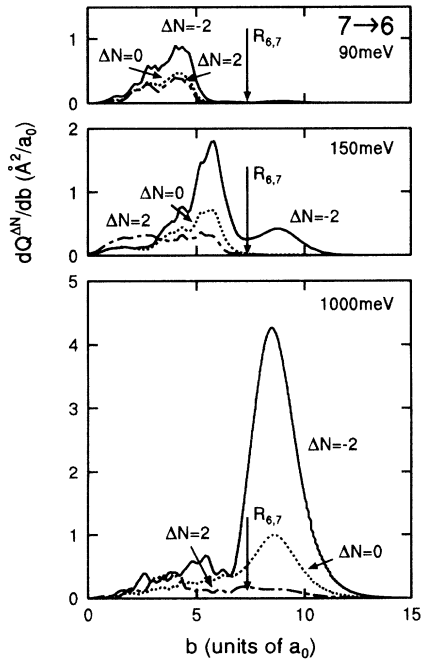

FIG. 18. Quantum-mechanical partial cross section $dQ^{\Delta N}_{6\leftarrow 7}/db$ as a function of the impact parameter b for the possible (even) changes $\Delta N = N_l - N_k$ of the rotational quantum number N of the relative nuclear motion, for collision energies E=90, 150, and 1000 meV, respectively. An averaging procedure over at maximum five values of the total angular momentum is applied to remove the fast Stückelberg oscillations. The arrow points to the position R_x of the avoided crossing. Note the clear preference for $\Delta N = -2$, even at lower energy, and the long-range contributions, dominant at higher energy.

and the trajectory followed and is in first approximation independent of the magnitude of g. We, therefore, expect only minor variations in the energy dependence of the cross-section magnitude. A strong decrease by almost a factor 2 is observed however. The lack of experimental data on the $|M_J|$=1 orientation is a nuisance in this respect.

$\{\alpha_5\} \rightarrow \{\alpha_8, \alpha_9\}$ *transitions.* For the $\{\alpha_5\} \rightarrow \{\alpha_8\}$ and $\{\alpha_5\} \rightarrow \{\alpha_9\}$ transitions, the cross-section magnitude, polarization effect, and their energy dependence are quite similar (see Fig. 11). This points to a strong coupling of the $\{\alpha_8\}$ and $\{\alpha_9\}$ state in the collision process, not present in the current semiclassical model. In Fig. 19 the quantum-mechanical partial cross sections $dQ^{\Delta N}_{8\leftarrow 5}/db$ and $dQ^{\Delta N}_{9\leftarrow 5}/db$ at a collision energy of 1000 meV are presented, respectively. The $\{\alpha_5\} \rightarrow \{\alpha_9\}$ transition shows a clear preference for ΔN=2 and even ΔN=4 in the region around $b = 7a_0$. These preferences are far more clear cut than any preference for the $\{\alpha_5\} \rightarrow \{\alpha_8\}$ transition. If we assume the $\{\alpha_5\} \rightarrow \{\alpha_9\}$ transition takes place via the $\{\alpha_8\}$ state, this difference in the partial cross sections points to the involvement of the "radial matching" mechanism in the transition from the $\{\alpha_8\}$ state to the $\{\alpha_9\}$ state.

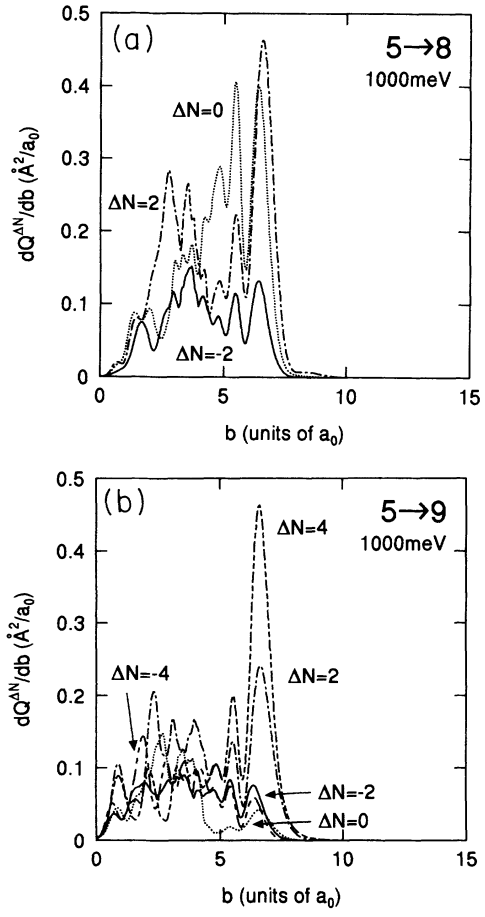

FIG. 19. Quantum-mechanical partial cross sections $dQ^{\Delta N}_{8\leftarrow 5}/db$ and $dQ^{\Delta N}_{9\leftarrow 5}/db$ as a function of the impact parameter b for the possible (even) changes $\Delta N = N_l - N_k$ of the rotational quantum number N at a collision energy of 1000 meV. The preference for ΔN=2 and even ΔN=4 for the $\{\alpha_5\} \rightarrow \{\alpha_9\}$ transition is more clear cut than any preference for the $\{\alpha_5\} \rightarrow \{\alpha_8\}$ transition. This points to a coupling by "radial matching" between the $\{\alpha_8\}$ and $\{\alpha_9\}$ state.

In conclusion, we find that the energy dependence of both the cross-section magnitude and the polarization effect, as disclosed by the TOF technique, indeed point to a serious short coming in the current semiclassical model. In this respect, a semiclassical model incorporating the "radial matching" transition mechanism is highly desirable.

IX. DETAILED BALANCING AND POLARIZATION ASYMMETRY

In Table VII cross-section magnitudes and polarization effects are compared as a function of the collision energy for the $\{\alpha_5\} \leftrightarrow \{\alpha_7\}$ reverse transition pair. The ratio $Q_{7\leftarrow 5}/Q_{5\leftarrow 7}$ tends towards unity for increasing energy. With equal statistical weights $(2J_k + 1)$ and the collision energy much larger than the atomic energy splitting ΔE_{57}=80.6 meV, this reflects the detailed balancing requirement. The polarization effect, however, clearly shows an asymmetry, even at the highest attainable collision energy. In essence, this reflects an experimental asymmetry: although the polarization of the initial state is well defined, the polarization of the final state is not observed. In more detail, detailed balancing is implied by the symmetry of the scattering S matrix ("microreversibility") and the incoherent "addition" of S-matrix elements, required to obtain the unpolarized cross section $Q_{l\leftarrow k}$. Also, the partial cross sections $dQ^{\Delta N}_{l\leftarrow k}/db$ and $dQ^{-\Delta N}_{k\leftarrow l}/db$ are identical for the same total (kinetic+electronic) energy.

A well defined initial polarization, however, implies a coherent superposition of initial partial waves, labelled by their rotational quantum number N_k. This coherence gives rise to cross products of S-matrix elements, differing in N_k, and finally results in an observable polarization effect. For the reverse $l \rightarrow k$ transition a different set of cross products is involved, now with S-matrix elements differing in N_l. Clearly, the symmetry of the S matrix has no implications on the ratio of polarization effects for a reverse transition pair.

The calculated partial cross section $dQ^{|M_7|}_{5\leftarrow 7}/db$ for E=1000 meV is depicted in Fig. 20 and reveals that the remaining polarization effect for the $\{\alpha_7\} \rightarrow \{\alpha_5\}$ transition, present in the calculations, but also observed experimentally (see Fig. 12), is due exclusively to a local peak in the $|M_k|$=0 contribution at b=6.5a_0. Possibly, this contribution is related to a similar peak present in the calculated partial cross section for the $\{\alpha_7\} \rightarrow \{\alpha_4\}$ transition, but now with $|M_k|$=1 (also depicted in Fig. 20).

The experimental data on the $\{\alpha_7\} \rightarrow \{\alpha_5, \alpha_4\}$ transitions clearly reveal a threshold behavior (see Fig. 12),

TABLE VII. Comparison of cross-section magnitude Q and polarization effect $\mathcal{P}$ as a function of the collision energy for the $\{\alpha_5\} \leftrightarrow \{\alpha_7\}$ reverse transition pair.

E (meV)	$Q_{7\leftarrow5}$ (Å^2)	$Q_{5\leftarrow7}$ (Å^2)	$Q_{7\leftarrow5}/Q_{5\leftarrow7}$	$\mathcal{P}_{7\leftarrow5}$	$\mathcal{P}_{5\leftarrow7}$	$\mathcal{P}_{7\leftarrow5}/\mathcal{P}_{5\leftarrow7}$
210	2.05	1.65	1.24	1.76	1.77	0.99
280	2.53	1.79	1.41	1.22	1.91	0.64
405	2.39	1.97	1.21	0.89	1.41	0.63
640	2.20	1.86	1.18	0.57	1.13	0.50
1190	2.36	2.23	1.06	0.63	1.19	0.53

as is to be expected from the endothermicities $\Delta E_{5,7}$=87 meV and $\Delta E_{4,7}$=106 meV, respectively. The $\{\alpha_5\}$ and $\{\alpha_4\}$ states are likely to be strongly coupled by the "radial matching" mechanism. Therefore, if the $\{\alpha_7\} \rightarrow \{\alpha_4\}$ transition takes place via the $\{\alpha_5\}$ state, we expect the TOF results to be alike, as is the case for the $\{\alpha_5\} \rightarrow \{\alpha_8, \alpha_9\}$ transitions. This is clearly not the case (see Fig. 12). A difference in this respect is that the $\{\alpha_7\} \rightarrow \{\alpha_4\}$ transition can only be made via the $\{\alpha_6\}$ state in the Ω=1 manifold, whereas the $\{\alpha_7\} \rightarrow \{\alpha_5\}$ transition can also be made directly in the Ω=0 manifold. A valid semiclassical model is needed to unravel the precise details of the transition dynamics involved.

Only the TOF results for $\{\alpha_5\} \rightarrow \{\alpha_6\}$ transition can qualitatively be understood directly with the current semiclassical model. This transition is due to a high reference velocity crossing v_{56}=2150 m/s at R_x=6.90a_0 in the "inner" region of the Ω=1 manifold. Partial cross sections $dQ^{|M_k|}_{6\leftarrow5}/db$ are given in Fig. 21 for collision energies E=150, 350, and 650 meV, respectively. With increasing energy, first the maximum attainable value of p_{kl} rises. Second, a shift of the main contribution towards larger impact parameters is observed, where the local radial velocity remains closer to the optimum value. Third, a (small) long-range contribution arises at high energy. A continuously increasing cross-section magnitude results, in agreement with the experimental results (see Fig. 9). Geometric Ω conservation at small impact parameters is mainly responsible for the calculated polarization effect, with polarization scrambling occuring at the larger

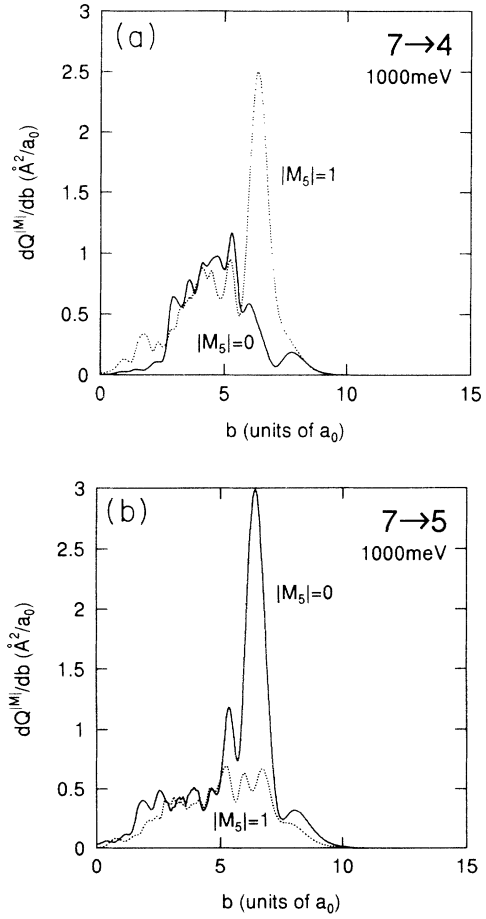

FIG. 20. Quantum-mechanical partial cross sections $dQ^{|M_7|}_{5\leftarrow7}/db$ and $dQ^{|M_7|}_{4\leftarrow7}/db$ as a function of the impact parameter b for the possible initial orientations $|M_7|$ of $\mathbf{J}_7$ with respect to $\mathbf{g}$ at E=1000 meV. For both transitions the remaining polarization effect at higher energy is mainly due to a localized peak at $R = 6.5a_0$.

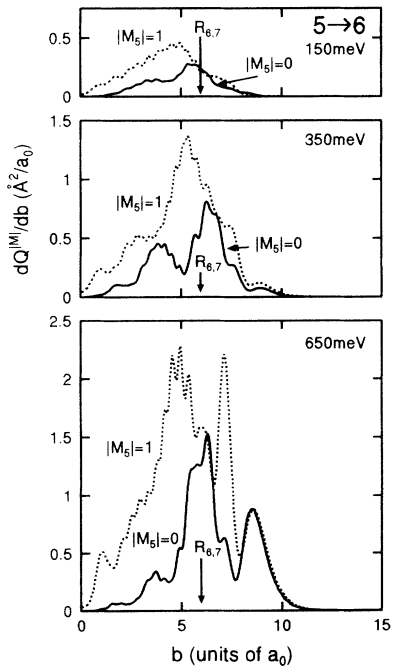

FIG. 21. Quantum-mechanical partial cross section $dQ^{|M_7|}_{5\leftarrow6}/db$ for collision energies E=150, 350, and 650 meV, respectively. The general features of the displayed calculations can be understood qualitatively with the current semiclassical model.

impact parameters. This also shows in the experimental results, which display a decreasing polarization effect with increasing energy.

X. CONCLUDING REMARKS

The TOF technique now is a mature tool to study the energy dependence of intramultiplet mixing for the Ne**-He system at superthermal energy. To allow a simple interpretation of the polarization effect, the method is only applied to J_k=1 initial states, specifically the $\{\alpha_5\}$ and $\{\alpha_7\}$ state. A wide spectrum of energy dependencies of the cross-section magnitude and polarization effect is observed. Definite evidence is found for a serious shortcoming in the current semiclassical model. The suggested "radial matching" mechanism is a prime candidate in explaining the observed discrepancies. In the development of an alternative semiclassical model and the eventual adaptation of the model potentials it uses as input, the presented data set offers a rigorous test bed.

[1] D. Hennecart, Ph.D. thesis, Université de Caen, Caen, France, 1982 (unpublished).

[2] D. Hennecart and F. Masnou-Seeuws, J. Phys. B **18**, 657 (1985).

[3] M.P.I. Manders, W.B.M. van Hoek, E.J.D. Vredenbregt, G.J. Sandker, H.C.W. Beijerinck, and B.J. Verhaar, Phys. Rev. A **39**, 4467 (1989).

[4] E.E.B. Campbell, H. Schmidt, and I.V. Hertel, Adv. Chem. Phys. **72**, 37 (1988).

[5] C.T. Rettner and R.N. Zare, J. Chem. Phys. **75**, 3636 (1981); **77**, 2416 (1982).

[6] J.M. Mestdagh, J. Berlande, P. de Pujo, J. Cuvellier, and A. Biner, Z. Phys. A **304**, 3 (1982).

[7] J.P. Visticot, P. de Pujo, O. Sublemontier, A.J. Bell, J. Berlande, J. Cuvellier, T. Gustavsson, A. Lallement, J.M. Mestdagh, P. Meynadier, and A.G. Suits, Phys. Rev. A **45**, 6371 (1992).

[8] R. Düren, E. Hasselbrink, and H. Tischer, Phys. Rev. Lett. **50**, 1983 (1983).

[9] R. Düren and E. Hasselbrink, J. Chem. Phys. **85**, 1880 (1986).

[10] W. Bussert, T. Bregel, R.J. Allan, M.W. Ruf, and H. Hotop, Z. Phys. A **320**, 105 (1985).

[11] W. Bussert, D. Neuschäfer, and S.R. Leone, J. Chem. Phys. **87**, 3833 (1987).

[12] E.E.B. Campbell, H. Hülser, R. Witte, and I.V. Hertel, Z. Phys. D **16**, 21 (1990).

[13] H.A.J. Meijer, Z. Phys. D **17**, 257 (1990).

[14] A.G. Suits, H.T. Hou, and Y.T. Lee, J. Phys. Chem. **94**, 5672 (1990).

[15] R.L. Robinson, L.J. Kovalenko, C.J. Smith, and S.R. Leone, J. Chem. Phys. **92**, 5260 (1990).

[16] J.P.J. Driessen, C.J. Smith, and S.R. Leone, Phys. Rev. A **44**, 1431 (1990); J. Phys. Chem. **95**, 8163 (1990).

[17] R.L. Dubs, P.S. Julienne, and F.H. Mies, J. Chem. Phys. **93**, 8784 (1990).

[18] M.P.I. Manders, J.P.J. Driessen, H.C.W. Beijerinck, and B.J. Verhaar, Phys. Rev. Lett. **57**, 1577 (1986); **57**, 2472 (1986).

[19] M.P.I. Manders, W.M.J. Ruyten, F. v.d. Beucken, J.P.J. Driessen, W.J.T. Veugelers, P.H. Kramer, E.J.D. Vredenbregt, W.B.M. van Hoek, G.J.Sandker, H.C.W. Beijerinck, and B.J. Verhaar, J. Chem. Phys. **89**, 4777 (1988).

[20] P.G.A. Theuws, H.C.W. Beijerinck, D.C. Schram, and N.F. Verster, J. Phys. E **15**, 573 (1982); P.G.A. Theuws, Ph.D. thesis, Eindhoven University of Technology, Eindhoven, 1981 (unpublished).

[21] M.J. Verheijen, H.C.W. Beijerinck, L.H.A.M. van Moll, J. Driessen, and N.F. Verster, J. Phys. E **17**, 904 (1984).

[22] M.P.I. Manders, W. Boom, H.C.W. Beijerinck, and B.J. Verhaar, Phys. Rev. A **39**, 5021 (1989).

[23] W. Boom, R.A.M.L. van Galen, B.J.P. Klaver, S.S. Op de Beek, J.T.A. Heier, H.C.W. Beijerinck, and B.J. Verhaar (unpublished).

[24] H.C.W. Beijerinck, G.H. Kaashoek, J.P.M. Beijers, and M.J. Verheijen, Physica C **121**, 425 (1983).

[25] F.C. van Nijmwegen, Internal Report No. VDF/CO 84-09, University of Technology, 1992, in Dutch (unpublished).

[26] H.C.W. Beijerinck and N.F. Verster, Physica C **111** , 327 (1981).

[27] H.C.W. Beijerinck, Ph.D. thesis, Eindhoven University of Technology, Eindhoven, 1975 (unpublished).

[28] C.A. Visser, J. Wolleswinkel, and J. Los, J. Phys. E **3**, 381 (1970).

[29] V.L. Hirshy and J.P. Aldridge, Rev. Sci. Instrum. **42**, 381 (1970).

[30] C.V. Nowikow and R. Grice, J. Phys. E **12**, 515 (1979).

[31] G. Comsa, R. David, and B.J. Schmacher, Rev. Sci. Instrum. **52**, 789 (1981).

[32] H. Baba and K. Sakurai, Rev. Sci. Instrum. **54**, 454 (1983).

[33] M.P.I. Manders, J.P.J. Driessen, H.C.W. Beijerinck, and B.J. Verhaar, Phys. Rev. A **37**, 3237 (1988).

[34] E.E. Nikitin, in *Chemische Elementar Prozesse*, edited by H. Hartmann and J. Heidelberg, (Springer Verlag, Berlin, 1968).